

# Dynamic movement history of the Iiyama slope failure revealed from seismic data

Masumi Yamada<sup>a</sup>, Yuki Matsushi<sup>a</sup>, Takanori Matsuzawa<sup>b</sup>

<sup>a</sup>Disaster Prevention Research Institute, Kyoto University

<sup>b</sup>National Research Institute for Earth Science and Disaster Resilience

---

## Abstract

The Iiyama slope failure occurred in the early morning of May 19, 2017, in Nagano Prefecture, central Japan. It caused a debris flow in the Idegawa River, resulting in the evacuation of the residents of the neighboring areas for half a year. Since the source was located in a mountainous area, the cause of the debris flow was not discovered immediately.

To investigate the mechanism of this slope failure, we performed a field survey and obtained aerial photos of the slope failure using an unmanned aerial vehicle. Additionally, we analyzed seismic data recorded by the surrounding stations, to identify the ground motion generated by the mass movements.

We found that the Iiyama slope failure involved two major mass movements: a large landslide and a subsequent debris flow triggered by the landslide. The movement of the landslide was recorded with long-period seismic waveforms, and the estimated force history showed a unidirectional movement from north to south for 50 s, reaching a maximum velocity of about 6.6 m/s. Following, debris flew for about 5 km from the top of the landslide source area. The initial collapse produced a large shaking with a short-period component, and the signal gradually decayed as the debris flow traveled along the river.

Our study shows that the two mass movements in the Iiyama slope failure generated ground motions with completely different frequencies. This suggests that the ground motions recorded by the seismometer are significant for understanding the movement mechanism of slope failure. The seismic signal, combined with the aerial photos, helps us to understand the dynamic movement history of the landslide.

## Highlights

- A complex mechanism of the slope failure was clarified by seismic data and UAV images
- Two mass movements were recorded in high- and low-frequency seismograms, respectively
- Seismic signals are useful for the detection and discrimination of slope failures

*Keywords:* Iiyama City, seismic signal, seismic waveform inversion, UAV image, debris flow, slope failure

---

## 1. Introduction

Slope failures are controlled by geologic structure and sometimes involve a complicated mechanism of collapse, as was the case of the slope failure that occurred in Iiyama City, Nagano Prefecture, Japan in 2017. The hillslope failure occurred in the early morning on May 19, 2017 (times in this paper are based on Japan Standard Time). Aerial photographs of the area show the trace of the debris flow and a large mass movement associated with the debris flow. The debris flew for about 5 km, and it was first observed by a local resident of the downstream area.

The failure generated a shaking of the ground, which was recorded by the surrounding seismic stations (Research Center on Landslides, 2017; Yamada et al., 2017). In general, seismic data are recorded continuously at a high sampling rate, so they are useful for estimating the timing and movement histories of slope failures (e.g. Hasegawa and Kanamori, 1987; Kawakatsu,

1989). In addition, seismic sensors record signals at a great distance, and thus their coverage is much wider (in the order of tens of kilometers) than those of other types of sensors, such as optical sensors or wire sensors (in the order of tens of meters).

Seismic data of mass movements can be analyzed following the deterministic approach or the stochastic approach. Long-period seismic waveforms (in general, longer than the period of microseisms, or about 10 s) are analyzed using the deterministic approach. The seismic waveform inversion technique estimates a force history of the mass movement by minimizing the difference between the synthetic waveform and the observed waveform. This approach provides information on the movement history, such as the time history of the force acting on the surface, velocity, mass, and the coefficient of friction (e.g. Brodsky et al., 2003; Favreau et al., 2010; Moretti et al., 2012; Allstadt, 2013; Yamada et al., 2013; Ekström and Stark,

2013; Yamada et al., 2018). On the other hand, short-period seismic waveforms are analyzed using the stochastic approach, since the waveforms are greatly affected by the small-scale seismic structure along the propagation path and it is difficult to calculate reliable synthetic waveforms. This approach uses the envelope of waveforms, arrival times, spectrograms, and power spectral density to obtain the location and size of an event, and the flow mechanics (e.g. Surifach et al., 2005; Yamada et al., 2012; Burtin et al., 2013, 2016; Chen et al., 2013; Chao et al., 2015; Walter et al., 2017; Lai et al., 2018). In this study, we combined these two approaches to extract information from seismic signals on the failure movement. We also performed a field survey and obtained aerial images using an unmanned aerial vehicle (UAV). By combining the seismic data with the aerial images, we investigated the complex mechanism of the Iiyama slope failure.

## 2. Site Description

The slope failure location is in the northern part of Nagano Prefecture, close to the boundary with Niigata Prefecture (Figure 1). A nearby resident found that the downstream area of the Idegawa River became muddy and reported this to the local authorities at 7:53 AM on May 19, 2017 (Iiyama City, 2017). The authorities confirmed that there was a large-scale hillslope failure in the upstream area of the river. There were no human casualties or property damage, but the downstream residents were ordered to evacuate for half a year (Iiyama City, 2017). Hiramatsu et al. (2017) analyzed the snow depth and precipitation data in this area and concluded that the cause of the landslide was most likely water originating from snowmelt.

The bedrock in the study area consists of Pleistocene volcanics, specifically andesitic pyroclastic rocks and lavas intercalated with layers of felsic tuff (Yanagisawa et al., 2001). This bedrock is covered by old and new landslide debris and a series of fluvial terrace deposits (Figure 2). The studied landslide occurred on a hillslope underlain by pyroclastic rocks and caused a subsequent debris flow, which traveled down about 5 km along the Idegawa River.

We performed a field survey on June 7-8, 2017, about three weeks after the slope failure occurred, and obtained aerial photos of the slope failure using an UAV. We made an orthophoto with commercial modeling software (Pix4Dmapper) that is shown in Figure 3(a).

The Iiyama slope failure consisted of two major mass movements. The western block (Figure 3(a)) moved from north-northwest to south-southeast and was deposited at the end of the slope (hereafter referred to as the landslide). The width of the mass was about 150 m and its length was about 400 m. This block was relatively undisturbed, and trees remained standing on the mass, which suggests its translational motion. Hiramatsu et al. (2017), based on the displacement of the control points on the undisturbed mass, estimated that the mass flew for a lateral distance of about 70 m. Note that there is a sharp vertical edge in the eastern boundary of the western landslide block, which intersects with the mountain ridge at an angle of about  $10^\circ$  (Fig-

ure 3(b)). The deposit of this landslide blocked the right-hand stream of the Idegawa River and created a landslide dam.

The material of the eastern block, which moved from west to east, supplied a debris flow that traveled along the left-hand stream of the Idegawa River. The source of the mass was about 100 m in width and 400 m in length. Most of the debris stopped at a debris barrier dam about 4 km downstream from the source, but some debris overflowed the dam, reaching the Chikuma River (Hiramatsu et al., 2017).

In Figure 3(c), we can observe flowlines (arrows) on the ground surface in the direction of the debris flow, so the upper right portion which is enclosed by the dotted line flowed as a debris flow. Figure 3(d) shows that the eastern part of the landslide was eroded and entrained by the debris flow, suggesting that the western block collapsed prior to the debris flow.

We estimated the total mass of the landslide by comparing the digital elevation models (DEMs) before and after the event. For this purpose, we used a three-dimensional DEM with 0.5-m grid spacing created from airborne Light Detection and Ranging (LiDAR) topographic surveys done by Nagano Prefecture after the slope failure (Figure 4), and a 5-m DEM made by photogrammetry before the slope failure (Geospatial Information Authority of Japan, 2017). Based on the mass thickness information shown in Figure 5, the source volume was estimated at  $1.2 \times 10^6 \text{ m}^3$  and the total mass of the displaced material at  $3 \times 10^9 \text{ kg}$ , assuming an average rock density of  $2.5 \times 10^3 \text{ kg/m}^3$  (Iwaya and Kano, 2005). Based on these DEMs and the envelopes shown in Figure 3(a), the volume of the western block was estimated at about 75% of the total volume.

The failed masses were a part of larger landslide body that can be identified on the pre-event topography. The local hillslope shows a low inclination ( $< 20^\circ$ ) and rugged topography as a result of the repeated movements of this long-lived landslide. A depression formed at the top of the slope before the failure event (Figure 4(b)), suggesting the preceding deformation of the sliding mass. The fractured and partly pulverized bedrock layers formed by the recent landslide activities covered the wide area of the hillslopes and they are described as younger landslide debris in Figure 2.

Boreholes had been drilled along a length profile of the western landslide body to understand its subsurface structures. Figure 5 shows the profiles of the boring cores drilled at six locations on the main body of the landslide. The local bedrock consists of tuff breccia, including andesite gravels in tuffaceous matrix, and intercalated tuff beds dipping southeast. The upper part of the bedrock had been chemically weathered, and it has been only slightly affected by the gravitational deformation of the entire hillslope. This bedrock was covered by massive landslide deposits, with heavily damaged structures due to the repeated landslide movements. The sliding surface of the 2017 failure event was formed at the base of these landslide deposits, with a maximum depth of 48 m below the ground, and it can be identified by the contrasting structures between the sliding mass and the immobile substrate.

### 3. Seismic Signals

The ground motion caused by the Iiyama slope failure was recorded by the surrounding seismic stations. Figure 1 shows the station distribution around the site of the failure. We used the F-net broadband seismic stations, short-period seismic stations (Hi-net and Japan Meteorological Agency), and high-sensitivity accelerometers collocated with the Hi-net short-period sensors. The high-sensitivity accelerometers consisted of two horizontal components, while the other sensors had three components.

Figure 6 shows the seismic signal at the closest station (N.MAKH) recorded by a high-sensitivity accelerometer. The distance between the station and the location of the failure event is about 8 km. Both the original accelerogram and displacement filtered between 0.01 and 0.1 Hz are shown. There is a clear difference in the signal arrival times between the two waveforms. The long-period displacement signal starts increasing at 60 s and records a harmonic pulse with a period of about 40 s. The acceleration signal at this period is relatively small, and it is suddenly amplified at 100 s. The signal is attenuated exponentially as a function of time, but a small signal continues for around five minutes (see Appendix Figure S1). Most of the energy in the acceleration record is contained in the frequencies between 1 and 4 Hz (Figure 6(c)).

These short-period characteristics are also observed at the other surrounding seismic stations as shown in Figure 7. This figure shows the velocity waveforms recorded by the short-period seismometers. To remove the high-frequency noise, we apply a fourth-order Butterworth low-pass filter with a cutoff frequency of 5 Hz. The amplitude of the waveform decays as a function of distance, but the signal of the landslide remains detectable as far as 40 km away. However, the records of distant stations have longer tails than the stations closest to the slope failure site due to the scattering of the short-period signals (Sato, 1977; Wu and Aki, 1988; Jing et al., 2014).

The long-period signals were recorded by the F-net broadband seismometer and the high-sensitivity accelerometers. Figure 8 shows the filtered displacement waveforms. We processed these records according to the following procedure. First, we removed the mean from the time series and corrected all waveforms for the instrumental response. A non-causal fourth-order Butterworth filter with a corner frequency of 0.014-0.1 Hz was applied. The filter window was selected so that much of the background noise was reduced without removing the landslide signal. We used a non-causal filter to avoid phase distortion in the shape of the landslide waveform. The data were integrated in the time domain to obtain the displacement waveforms. Figure 8 shows the consistent harmonic pulse in the waveforms of all stations, but the amplitudes of the EW and UD components are relatively small. We used these filtered displacement waveforms with a duration of 150 s starting from 6:36:40 AM, May 19, 2017, for the seismic waveform inversion in the next section.

### 4. Seismic Waveform Inversion

Long-period ground motion is less influenced by subsurface soil structure than short-period motion, and this helps extracting long-period source information on the landslide movement. In order to determine the landslide mechanism, we performed seismic waveform inversion (Kawakatsu, 1989; Brodsky et al., 2003; Yamada et al., 2013). The inversion technique estimates the force history acting on a fixed location by minimizing the difference between observed and synthetic waveforms. The synthetic waveforms are a convolution of the pre-computed Green's function and the force history. We performed a grid search in space to find the optimal location for explaining the observed seismic waveforms. The grid search was performed in an area of about 30 km  $\times$  30 km with a 5 km spacing (Figure 1).

We calculated Green's functions at each node using the discrete wavenumber method (Bouchon, 1979) and the Japan Meteorological Agency's (JMA) one-dimensional velocity structure model (Ueno et al., 2002). Based on the method of Nakano et al. (2008), we performed a seismic waveform inversion in the frequency domain and determined the best fitting three-component source time function of a single-force mechanism, assuming locations at each grid point. Then, the normalized residual of equation (7) found in Nakano et al. (2008), which is the difference between observed and synthetic waveforms normalized by the amplitude of the observed waveforms, for each node is used to determine the source location. Figure 1 shows the residual contour of this grid search which suggests that the best-fit source location is very close to the Iiyama slope failure site.

Since the spatial resolution of the grid search is rather coarse (5 km), in the next step we fixed the exact location of the source at the site of the Iiyama slope failure (36.99°N, 138.42°E) and repeated the waveform inversion. Figure 8 shows the optimal force history and the waveform fit. There is good agreement between observed and synthetic waveforms with a normalized residual of 0.07.

The force history in Figure 8(a) shows a clear harmonic signal at 55-100 s. This corresponds to a typical source time function for the landslide movement with relatively short travel distance (Brodsky et al., 2003; Yamada et al., 2013, 2018). It reflects the acceleration and deceleration process of the landslide movement. The Green's functions are dominated by surface waves and the vertical component of the force contributes significantly to the shape and amplitude of the (horizontal component) Rayleigh waves. Therefore, horizontal waveforms contain information about the vertical force, and with enough numbers and azimuthal coverage of stations, these data can be used to estimate the vertical force. To evaluate how well the vertical force was resolved from our dataset, we computed the model resolution matrix (Menke, 2018). We confirmed that they were identity matrices in all the frequency and the rank of the Green's function matrices was equal to the number of the unknown parameters (i.e., 3). This supports that all components were well resolved in our analysis.

The maximum force in the vector sum is estimated as

$2.1 \times 10^9$  N. The acceleration history can be obtained by dividing the force by the mass, and the velocity history is found by integrating the acceleration history. Assuming a constant mass (i.e., that the whole mass moved uniformly), the maximum estimated acceleration and velocity were  $0.69 \text{ m/s}^2$  and  $6.6 \text{ m/s}$ , respectively.

## 5. Discussion

The Iiyama slope failure was a unique landslide with both a substantial mass movement and a debris flow occurring closely in time and space. Based on the DEM model, there were two major blocks. The western block moved from NNW to SSE and was deposited at the valley bottom. The eastern block flowed along the river as a debris flow.

The western block slid on the bedrock of tuff-breccia, with a thickness of about 50 m (Nagano Prefecture, personal communication). Since the sliding surface had formed along the pre-existing geological structure, the mass was likely to move uniformly as a block in the translational direction. The moving direction of the landslide coincided with the dipping direction of the bedding locally (Figure 2).

The movement of the eastern body, which became a debris flow, succeeded that of the western block, since the debris flow excavated the slid mass of the western block (Figure 3(d)). Since the two movements occurred closely in time and space, we interpreted that the debris flow was triggered by the movement of the western block. Hiramatsu et al. (2017) observed multiple springs flowing from the side scarp of this eastern part immediately after the failure. The abundant supply of subsurface water may have promoted the movement of the debris flow.

The force history estimated from the long-period waveforms shows a simple unidirectional mass movement. The particle motion in the horizontal plane and the section along the sliding direction are in good agreement with regard to the direction of movement (Figures 4 and 9). The first positive pulse in the NS direction (Figure 8(a)) corresponds to the acceleration at the beginning of sliding, and the second negative pulse corresponds to the deceleration due to the mass block reaching the valley (Yamada et al., 2013).

Signals of debris flows tend to appear in the short-period ground motions (Burtin et al., 2016). The ground motion is essentially produced by the impact between particles and the ground within the channel (Lai et al., 2018). The frequency of the signal recorded by the regional network is about 1-5 Hz in general (Chen et al., 2013; Allstadt et al., 2018), but it may be higher if the station were close to the source (Burtin et al., 2016; Walter et al., 2017; Lai et al., 2018), due to the larger attenuation in high frequencies. The seismic signal of the debris flow tends to have an emergent onset, and the duration is in the order of tens of minutes, depending on the flow distance (Burtin et al., 2016; Walter et al., 2017; Lai et al., 2018; Allstadt et al., 2018).

Compared to past studies, the short-period ground motion in Figure 6(a) shows a sharp peak and decays exponentially as a function of time. Since the source-station distance is large

compared to the migration of the source, the amplitude change may reflect the flow process. Based on this assumption, the large amplitude may correspond to the initiation process from the collapse to the debris flow, and the long tail of the waveform suggests that the debris flowed along the river. These signals did not appear in the long-period component, since the mass of each particle was too small to produce the necessary momentum on the ground surface.

We estimated that the landslide started moving at 6:37:35 AM, and continued for about 50 s. The debris flow was triggered by the landslide at 6:38:20 AM, the large amplitude of the seismic signal lasted around 3 minutes, and the amplitude went back to its original noise level after 5 minutes (see Appendix Figure S1). Hiramatsu et al. (2017) described the stream profile and change in the riverbed heights obtained from the airborne laser surveys before and after the event. There is a substantial change in the riverbed between the source area and the debris barrier dam (Figure 2). This suggests that the seismic signals of the debris flow were produced efficiently in this 4-km stretch. Therefore, the average speed of the debris flow in this section is estimated at 13 m/s. Hiramatsu et al. (2017) estimated that the velocity of the subsequent debris flow at 2:40 PM on May 22 was 11 m/s across the lowest 1 km of its flow range. Assuming the upstream area had a higher slope and larger velocity, this number is consistent with our estimated velocity of the debris flow. The velocity may have changed if the debris flow was stretched while traveling or if it occurred successively.

The complex mechanism of the Iiyama slope failure was clarified by seismic signals and UAV images. The seismic stations in the study area were originally installed for constructing an earthquake catalog, but they have also proven useful for the analysis of geotechnical hazards. By using a UAV, high-quality and high-resolution aerial images are easily obtained. With these aerial images, researchers can conduct photogrammetry using sophisticated structure-from-motion software (e.g. Walter et al., 2009; Niethammer et al., 2012). This research is unique, because the complex movement of the slope failure was analyzed using remote sensors at relatively low cost and in a short time, compared to conventional field surveys. These remote tools are expected to be very effective in the quick investigation and mechanism clarification of future geotechnical hazards occurring at inaccessible locations.

## 6. Conclusions

We investigated the complex mechanism of the Iiyama slope failure by obtaining field data and aerial photos through a field survey three weeks after the incident, and by analyzing the seismic signal of the slope failure. Our aim was to extract the slope failure's timing and movement history.

We found that the Iiyama slope failure consisted of two major mass movements: a large landslide and a subsequent debris flow triggered by the landslide. These two movements were recorded at the surrounding seismic stations at different frequencies. The combination of the long-period and short-period seismic waveforms reveals the timing and types of the recorded

mass movements. The UAV provides information on the geology and topography of the surface process and the aerial photos can also be used for creating a DEM if a high-resolution DEM is not available.

Our study shows that the two mass movements in the Iiyama slope failure generated ground motions with completely different frequencies. This suggests that the ground motions recorded by the seismometer are significant for understanding the movement mechanism of the slope failure. The seismic signal, combined with drone aerial photos, helps us to understand the dynamic movement history of the landslide.

## Acknowledgements

We acknowledge the National Research Institute for Earth Science and Disaster Resilience (NIED) and the Japan Meteorological Agency (JMA) for the use of seismic data. High-resolution DEM data were provided by the Hokushin Construction Office, Nagano Prefecture. We thank the Hokushin Regional Development Bureau, Nagano Prefecture, for providing geological information, including profiles of boring cores. We also thank Dr. Hiroyuki Kumagai in Nagoya university and Dr. Masaru Nakano in Japan Agency for Marine-Earth Science and Technology (JAMSTEC), who provided us with a computer program of the waveform inversion. We used generic mapping tools (GMT) to draw the figures (Wessel and Smith, 1991).

## References

Allstadt, K. (2013). Extracting source characteristics and dynamics of the August 2010 Mount Meager landslide from broadband seismograms. *Journal of Geophysical Research: Earth Surface*, 118(3):1472–1490.

Allstadt, K. E., Matoza, R. S., Lockhart, A., Moran, S. C., Caplan-Auerbach, J., Haney, M., Thelen, W. A., and Malone, S. D. (2018). Seismic and acoustic signatures of surficial mass movements at volcanoes. *Journal of Volcanology and Geothermal Research*.

Bouchon, M. (1979). Discrete wave number representation of elastic wave fields in three-space dimensions. *Journal of Geophysical Research*, 84(B7):3609–3614.

Brodsky, E., Gordeev, E., and Kanamori, H. (2003). Landslide basal friction as measured by seismic waves. *Geophysical Research Letters*, 30(24):2236.

Burtin, A., Hovius, N., Milodowski, D. T., Chen, Y., Wu, Y., Lin, C., Chen, H., Emberson, R., and Leu, P. (2013). Continuous catchment-scale monitoring of geomorphic processes with a 2-D seismological array. *Journal of Geophysical Research: Earth Surface*, 118(3):1956–1974.

Burtin, A., Hovius, N., and Turowski, J. M. (2016). Seismic monitoring of torrential and fluvial processes. *Earth Surface Dynamics*, 4(2).

Chao, W.-A., Wu, Y.-M., Zhao, L., Tsai, V. C., and Chen, C.-H. (2015). Seismologically determined bedload flux during the typhoon season. *Scientific reports*, 5:8261.

Chen, C.-H., Chao, W.-A., Wu, Y.-M., Zhao, L., Chen, Y.-G., Ho, W.-Y., Lin, T.-L., Kuo, K.-H., and Chang, J.-M. (2013). A seismological study of landquakes using a real-time broad-band seismic network. *Geophysical Journal International*, 194(2):885–898.

Ekström, G. and Stark, C. P. (2013). Simple scaling of catastrophic landslide dynamics. *Science*, 339(6126):1416–1419.

Favreau, P., Mangeney, A., Lucas, A., Crosta, G., and Bouchut, F. (2010). Numerical modeling of landquakes. *Geophysical Research Letters*, 37:L15305.

Geospatial Information Authority of Japan (2017). Basemap information download service.

Hasegawa, H. and Kanamori, H. (1987). Source mechanism of the magnitude 7.2 Grand Banks earthquake of November 1929: Double couple or submarine landslide? *Bulletin of the Seismological Society of America*, 77(6):1984–2004.

Hiramatsu, S., Ishida, K., Kanazawa, A., Gonda, Y., Sawa, Y., Tsutsumi, D., Nagayama, T., Fukuyama, T., Mantoku, M., Miike, T., Morishita, A., Yamajima, K., and Yamada, Y. (2017). Slope failure and subsequent debris flow occurrence on May 2017 at Iiyama, Nagano, Japan. *Journal of the Japan Society of Erosion Control Engineering*, 70(3):41–50.

Iiyama City (2017). Response to the slope failure in Teruoka, Iiyama City. <http://www.city.iiyama.nagano.jp/soshiki/kikikanribousai/bousaisuibou/saigaiinfo/20170520sanpuku>, (last accessed May 8, 2019).

Iwaya, T. and Kano, K. (2005). Rock densities for the geologic units in the Japanese islands: an estimate from the database PROCK (Physical Properties of Rocks of Japan). *Journal of the Geological Society of Japan*, 111(7):434.

Jing, Y., Zeng, Y., and Lin, G. (2014). High-frequency seismogram envelope inversion using a multiple nonisotropic scattering model: Application to aftershocks of the 2008 wells earthquake. *Bulletin of the Seismological Society of America*, 104(2):823–839.

Kawakatsu, H. (1989). Centroid single force inversion of seismic waves generated by landslides. *Journal of Geophysical Research*, 94(B9):12363–12374.

Lai, V. H., Tsai, V. C., Lamb, M. P., Ulizio, T. P., and Beer, A. R. (2018). The seismic signature of debris flows: Flow mechanics and early warning at Montecito, California. *Geophysical Research Letters*.

Menke, W. (2018). Geophysical data analysis: Discrete inverse theory. Academic press.

Moretti, L., Mangeney, A., Capdeville, Y., Stutzmann, E., Huggel, C., Schneider, D., and Bouchut, F. (2012). Numerical modeling of the Mount Steller landslide flow history and of the generated long period seismic waves. *Geophysical Research Letters*, 39:L16402.

Nakano, M., Kumagai, H., and Inoue, H. (2008). Waveform inversion in the frequency domain for the simultaneous determination of earthquake source mechanism and moment function. *Geophysical Journal International*, 173(3):1000–1011.

Niethammer, U., James, M., Rothmund, S., Travelletti, J., and Joswig, M. (2012). UAV-based remote sensing of the Super-Sauze landslide: Evaluation and results. *Engineering Geology*, 128:2–11.

Research Center on Landslides, DPRI, Kyoto University (2017). Seismic waveforms produced at around the slope failure in Iiyama City, Nagano Prefecture. [http://landslide.dpri.kyoto-u.ac.jp/report/2017/20170522nagano\\_landslide.pdf](http://landslide.dpri.kyoto-u.ac.jp/report/2017/20170522nagano_landslide.pdf), (last accessed May 8, 2019).

Sato, H. (1977). Single isotropic scattering model including wave conversions simple theoretical model of the short period body wave propagation. *Journal of Physics of the Earth*, 25(2):163–176.

Suriñach, E., Vilajosana, I., Khazaradze, G., Biescas, B., Furdada, G., and Vilaplana, J. (2005). Seismic detection and characterization of landslides and other mass movements. *Natural Hazards and Earth System Scienc.*, 5:791–798.

Ueno, H., Hatakeyama, S., Aketagawa, T., Funasaki, J., and Hamada, N. (2002). Improvement of hypocenter determination procedures in the Japan Meteorological Agency. *Quarterly Journal of Seismology*, 65:123–134.

Walter, F., Burtin, A., McArdell, B. W., Hovius, N., Weder, B., and Turowski, J. M. (2017). Testing seismic amplitude source location for fast debris-flow detection at illgraben, switzerland. *Natural Hazards and Earth System Sciences*, 17(6):939–955.

Walter, M., Niethammer, U., Rothmund, S., and Joswig, M. (2009). Joint analysis of the Super-Sauze (French Alps) mudslide by nanoseismic monitoring and UAV-based remote sensing. *first break*, 27(8).

Wessel, P. and Smith, W. (1991). Free software helps map and display data. *Eos*, 72(441):445–446.

Wu, R.-S. and Aki, K. (1988). *Multiple scattering and energy transfer of seismic waves—Separation of scattering effect from intrinsic attenuation II. Application of the theory to Hindu Kush region*, pages 49–80. Springer.

Yamada, M., Matsushi, Y., Chigira, M., and Mori, J. (2012). Seismic recordings of landslides caused by typhoon Talas (2011), Japan. *Geophysical Research Letters*, 39(13):L13301.

Yamada, M., Kumagai, H., Matsushi, Y., and Matsuzawa, T. (2013). Dynamic landslide processes revealed by broadband seismic records. *Geophysical Research Letters*, 40(12):2998–3002.

Yamada, M., Kamo, M., and Matsushi, Y. (2017). Report on the damage survey for the May 19 2017 Iiyama slope failure. <http://www.eqh.dpri.kyoto-u.ac.jp/~masumi/eq/iiyama2017/>, (last accessed May 8, 2019).

Yamada, M., Mangeney, A., Matsushi, Y., and Matsuzawa, T. (2018). Estimation of dynamic friction and movement history of large landslides. *Landslides*, 15(10):1963–1974.

Yanagisawa, Y., Kaneko, T., Akahane, S., Awata, Y. Kamai, T., and Tsuchiya, N. (2001). Geology of the Iiyama district, with geological map at 1:50,000. *Geological Survey of Japan*, 144p, (in Japanese).

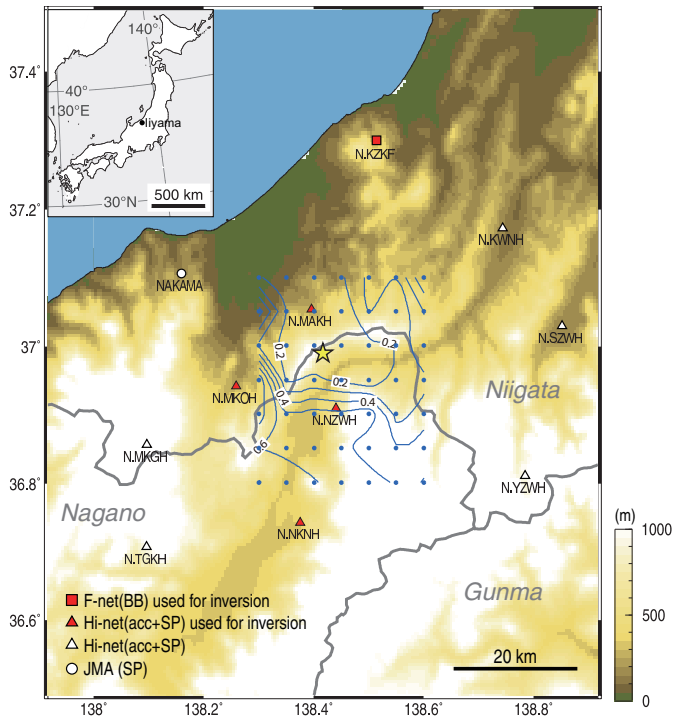


Figure 1: Map with the locations of the seismic stations. The star shows the landslide location, triangles show Hi-net locations, the circle shows a JMA short-period (SP) seismic station, and the square shows an F-net broadband (BB) station. The filled symbols represent the stations used for the waveform inversion. The background color shows the elevation, and thick solid lines show the prefecture boundary. The black dots show the locations of the grid search and the contour lines show the residuals of the grid search. The inset shows the map of Japan and the location of the slope failure.

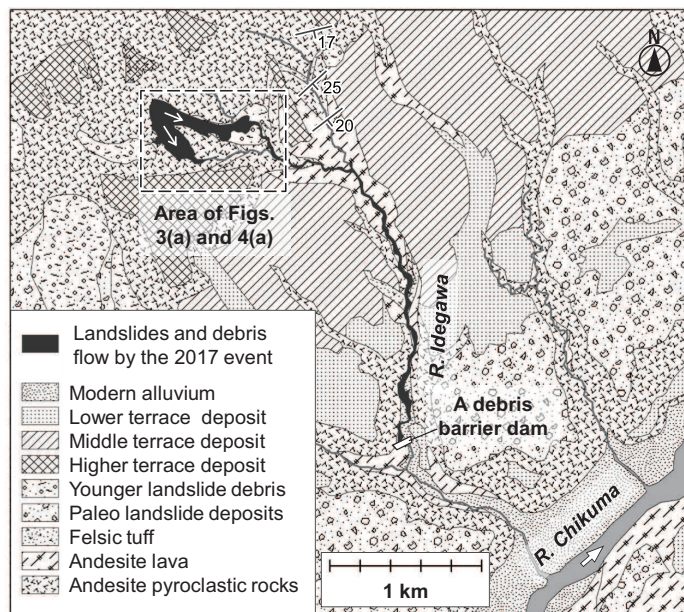


Figure 2: Geological map of the study area (modified after Yanagisawa et al. (2001)). The numbers show the strike and dip of the strata.



Figure 3: Photos taken using UAV images (June 8, 2017). The white solid lines show the envelope of the landslide, and the white dotted lines show the envelope of the debris flow. The white arrows show the direction of the flowline on the ground surface. (a) The orthophoto generated by the software. The locations and directions of photos (b)-(d) are indicated with black arrows. (b) Photo of the scarp at the eastern edge of the landslide. (c) Photo of the source head of the landslide. (d) Photo of the scarp made by the debris flow.

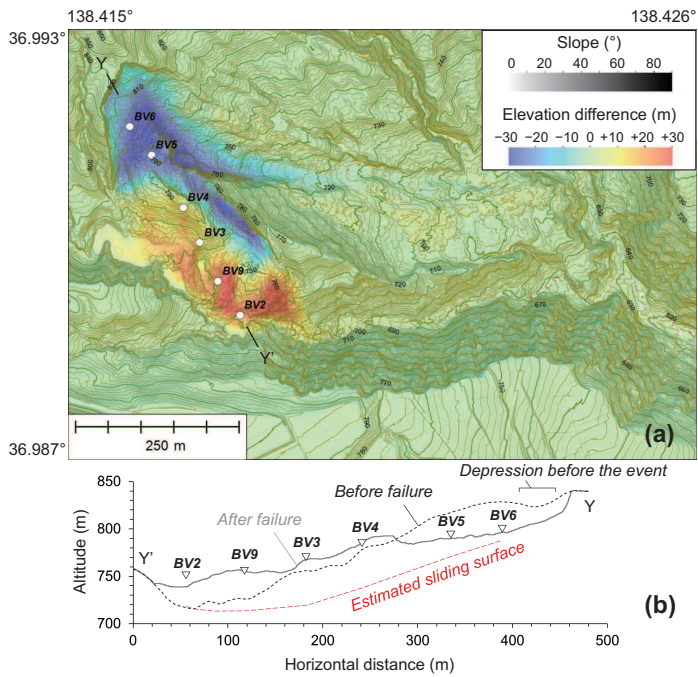


Figure 4: Topography of the Iiyama landslide. (a) Elevation change at the Iiyama landslide. The contours show the DEM after the landslide (July 3, 2017). Circles show the locations of the boring cores. (b) Vertical section along the Y-Y' segment before and after the failure. (courtesy of the Hokushin Regional Development Bureau)

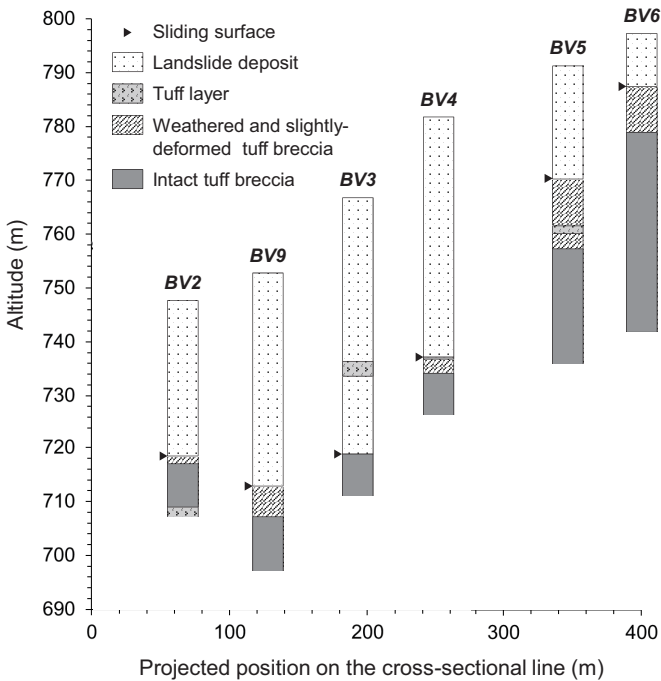


Figure 5: Profiles of six boring cores drilled on the main body of the landslide (courtesy of the Hokushin Regional Development Bureau). The locations are shown in Figure 4.

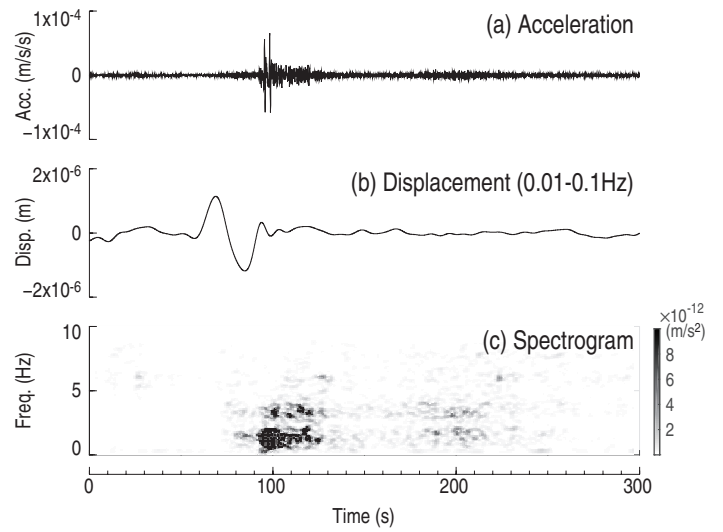


Figure 6: Seismic records of the Iiyama landslide at N.MAKH station in NS component. The origin time is 6:36:40 AM, May 19, 2017. (a) Original high-sensitivity accelerometer record, (b) filtered displacement record with a non-causal fourth order Butterworth filter between 0.01 and 0.1 Hz, and (c) spectrogram of the acceleration record. Each segment for the fast Fourier transform has 128 samples and overlaps 112 samples.

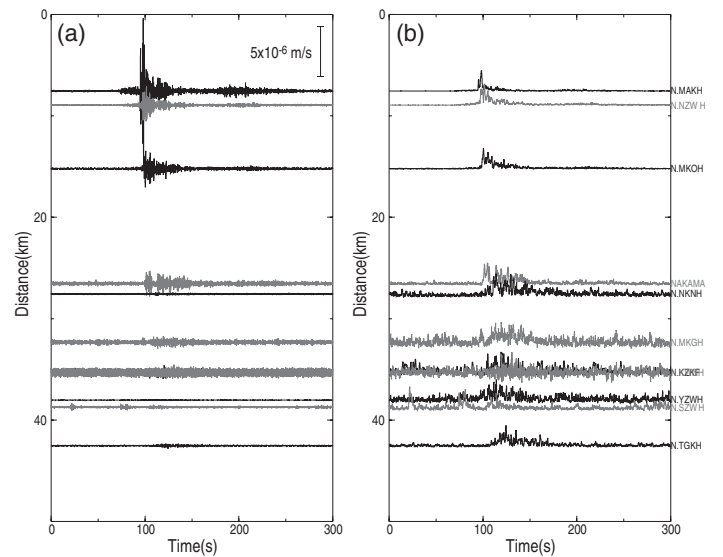


Figure 7: Seismic records of the Iiyama landslide recorded by the Hi-net and the JMA seismic network in the NS component. (a) 5 Hz low-pass filtered waveforms and (b) normalized envelopes. The origin time is 6:36:40AM, May 19, 2017. Adjacent seismograms are shown alternately in black and gray for clarity.

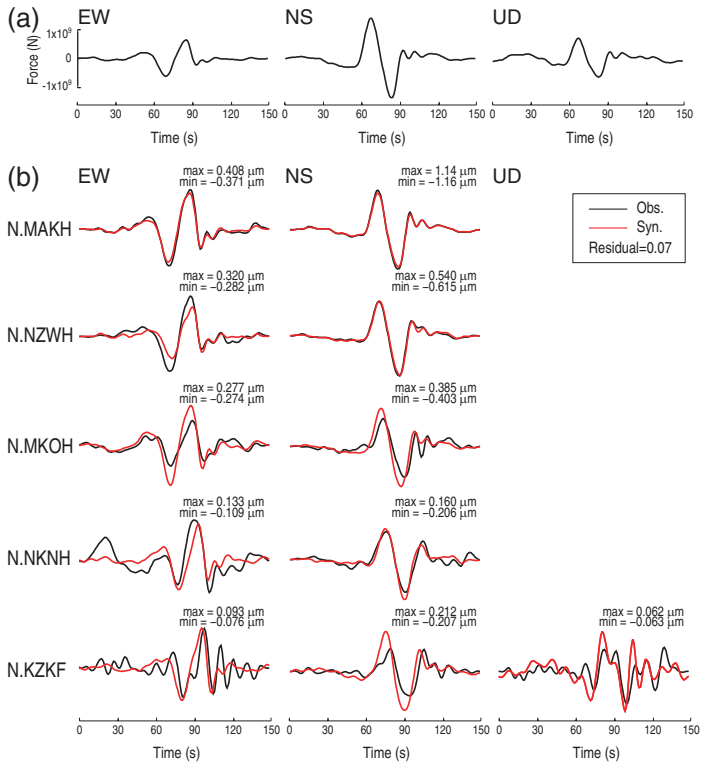


Figure 8: Seismic waveforms of the Iiyama landslides with a band-pass filter at 0.014-0.1 Hz. The origin time is 6:36:40AM, May 19, 2017. (a) Estimated single-force source time functions for the EW, NS, and UD components. (b) Displacement waveform fits between observed (black) and synthetic (red) data obtained from the source inversion. The letters on the left show the station code, and the numbers at the top right show the largest amplitude of the two waveforms.

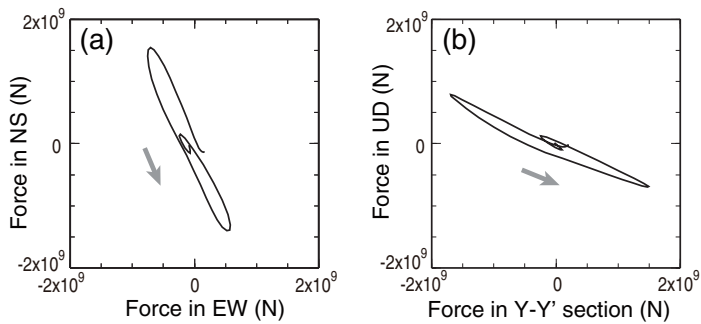


Figure 9: Particle motion of the source time function between 55 and 100 s in Figure 8(a). Gray arrows show the direction of the particle motion. (a) Horizontal section and (b) vertical section along the Y-Y' segment (Figure 4(a)).